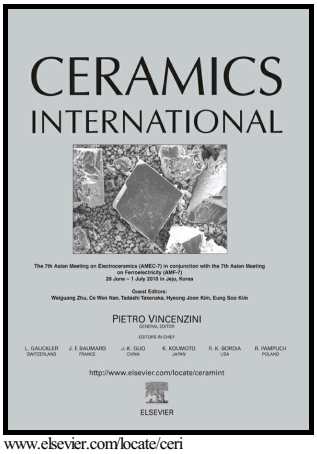

www.elsevier.com/locate/ceri

Structural, electrical and relaxor properties of Sc-In solid solution in tetragonal tungsten bronze ceramics

Andrei Rotaru, Finlay D. Morrison

PII: S0272-8842(18)32670-1
DOI: https://doi.org/10.1016/j.ceramint.2018.09.202
Reference: CERI19601

To appear in: *Ceramics International*

Cite this article as: Andrei Rotaru and Finlay D. Morrison, Structural, electrical and relaxor properties of Sc-In solid solution in tetragonal tungsten bronze ceramics, *Ceramics International,* https://doi.org/10.1016/j.ceramint.2018.09.202

Structural, electrical and relaxor properties of Sc-In solid solution in tetragonal tungsten bronze ceramics

Andrei Rotaru[1,2,3], Finlay D. Morrison[1]*

[1]*EaStCHEM Research School of Chemistry, University of St Andrews, North Haugh, KY16 9ST, St Andrews, Fife, Scotland, United Kingdom*

[2]*University of Craiova, Faculty of Horticulture, Department of Horticulture and Food Science, Str. A.I. Cuza, Nr. 13, Craiova, Romania*

[3]*INFLPR – National Institute for Laser, Plasma and Radiation Physics, Laser Department, Bvd. Atomistilor, Nr. 409, 077125, Măgurele (Ilfov), Bucharest, Romania*

*Corresponding author: **finlay.morrison@st-andrews.ac.uk**, Telephone: +441334463855

Abstract

The electrical properties of a family of tetragonal tungsten bronze (TTB) materials, $Ba_6Sc_{1-x}In_xNb_9O_{30}$ (x = 0.25, 0.5, 0.75), which display relaxor properties were characterised using high-temperature impedance spectroscopy and low-temperature dielectric spectroscopy. All powders were synthesized at 1250 °C (24 hours) + 1350 °C (6.5 hours), while the pellets were further sintered at 1350 °C (12 hours). At high temperature, the electrical conductivity in all samples is dominated by a single response, attributed to the bulk response, while the subtle asymmetry of the imaginary impedance peak suggests a minor contribution of the grain boundary response. In general, the Sc-In solid solutions samples exhibit similar electrical behaviour to the Sc compound, x = 1 reported previously (*Ceram. Int.* **2016**, 42, 11810-11821). At low temperature all compounds exhibit frequency dependent relaxor behaviour. With increasing the content of In, the dielectric peaks are more asymmetric and the curves flatten more at temperatures above the transition temperature. The dipole freezing temperature, T_{VF}, determined by Vogel-Fulcher (VF) analysis does not simply increases linearly as a function of M^{3+} (Sc^{3+},In^{3+}) cation size, the extrapolation of VF-like curves results in considerably different values when compared to those found previously, since the acquired dielectric data are very sensitive to preparative conditions.

Keywords: electrical conduction, microstructure, relaxor behaviour, tetragonal tungsten bronzes, Vogel-Fulcher analysis.

1. Introduction

Tetragonal tungsten bronzes (TTBs) are ceramic materials derived from the common perovskite unit, which due to their versatile structure may exhibit very interesting and useful electrical, optical, magnetic, catalytic or photocatalytic properties, with various applications in the optoelectronic, energy conversion or chemical sectors [1-5]. Recently, they received much of attention in the research community mainly due to their versatile structure [1,6-8]: $(A1)_2(A2)_4(C)_4(B1)_2(B2)_8O_{30}$, which allows for the inclusion of particular metals into the five different types of TTB sites [9] and offers the possibility of adjusting both electric and magnetic behaviour [10,11]. The polyhedral representation of the tetragonal tungsten bronze (TTB) aristotype structure – viewed down the c-axis – and detailed information regarding the occupation possibilities for the five different TTB sites, may be found in several works [12,13]. Thus, it is aimed for the fine tuning of properties in order to develop new phases [6,14] ranging from ferroelectrics [15-17] to microwave dielectrics [18,19] and to ionic conductors [20], ultimately for the discovery of the so-much desired room-temperature multiferroic material.

However, during the last few years, the research was mostly directed to the synthesis and characterisation of novel TTB ferroelectric and ferroelectric-related materials [8-17,21-26], with $Sr_5Nb_{10}O_{30}$-$Ba_5Nb_{10}O_{30}$ system (SBN) [27] and $Ba_6FeNb_9O_{30}$ (BFNO) [28-31] as the main starting point. These ceramic materials exhibit actually relaxor ferroelectric/dielectric phenomena [6,12,32-37]; in the BFNO-related materials, it was shown that due to the variable oxidation state of Fe (Fe^{3+}/Fe^{2+}) appear oxygen vacancy gradients, and both low temperature dielectric spectroscopy and high temperature impedance spectroscopy measurements indicated more electroactive regions than anticipated [9,38]. The compositional variables give however even to simple single-phase ceramic materials a complex behaviour, therefore the structural, electrical and relaxor properties of TTBs have to be deeply investigated [10,11,13,21].

Starting from BFNO and taking into consideration the problems stated above, in order to avoid these additional complications, the TTBs family of relaxors $Ba_6M^{3+}Nb_9O_{30}$, where the trivalent species do not have variable oxidation states (*e.g.* Ga^{3+}, Sc^{3+}, In^{3+}) was synthesised and reported [6,9,12]. The slowing of dipolar response on cooling and the eventual "locking" of the B-cation displacements along the *c*-axis, (*i.e.* dipole freezing) was observed [12], while the dynamics of dielectric relaxation of dipoles was extensively investigated by Vogel-Fulcher (VF); the VF fits proved to be very sensitive on the processing parameters [6,36], and the main relaxor behaviour being accompanied by both elastic and anelastic relaxations, as observed by resonance ultrasound spectroscopy (RUS) [37].

In one of our recent study [13], the ceramic microstructure for three compositions of $Ba_6MNb_9O_{30}$ (M=Ga, Sc, In) was investigated in relation with the high temperature impedance spectroscopy studies, in order to identify the electroactive regions present within these materials (by calculating the capacitances and the resistances of both grain boundaries and bulk parts), and to understand their influence on the macroscopic dielectric response. From the activation energy values of the electrical conduction process it was evident that for $Ba_6GaNb_9O_{30}$ and $Ba_6InNb_9O_{30}$ the conduction mechanisms are dominated by the bulk response, while for $Ba_6ScNb_9O_{30}$ the grain boundary effects mix strongly with the bulk response making it hard to clearly assign a specific grain boundary contribution [6,13]. This result relates to the microstructural observations: to the Ga and In analogues which had pellets that revealed good, dense internal microstructures, with well-bonded grains and only discrete porosity, the majority of the grains almost were completely fused into big lumps of material with irregular shape and formed continuous interfaces. While for the Sc analogue, the pellet did not have a very good internal microstructure, with many small and poorly-bonded grains, gathered in agglomerates (linked by some independent small grains with irregular shapes and dimensions) and also with independent small grains exceeding and randomly distributed, resulting in significant continuous porosity and poorly defined grain boundary regions [6,13].

In this paper we aim to continue this investigation; the full structural, morphological and dielectric characterisation of B-site substituted Sc-In solid solutions with general formula: $Ba_6Sc_{1-x}In_xNb_9O_{30}$ (x = 0.25, 0.5, 0.75) TTB materials is discussed. The investigation of the structural evolution and of the characteristic temperature parameters of the main relaxation process for each sample is interesting in the wider context of understanding the behaviour of Sc and In analogues, and of course as part of the $Ba_6M^{3+}Nb_9O_{30}$ series [6].

2. Experimental

2.1. Materials

Three ceramic compositions within the solid solutions of $Ba_6MNb_9O_{30}$ (M = Sc, In) with the formula: $Ba_6Sc_{1-x}In_xNb_9O_{30}$ (x = 0.25, 0.5, 0.75) [6] were synthesised by standard solid-state techniques. Stoichiometric ratios of dried $BaCO_3$, Nb_2O_5, In_2O_3, (all Aldrich, 99+%) and Sc_2O_3 (Stanford Materials Corporation, 99.999%) were ball milled in ethanol until homogenized (5 mins at 400 rpm, using a Fritsch Pulverisette 7 system with agate mortar and balls). Powders were placed on platinum foil in alumina boats inside a muffle furnace at 600 °C (static air atmosphere) and fired initially to 1000 °C, left to decarbonate for 1 hour, and further fired for 12 hours at 1250 °C (heating rates: 10 $K \cdot min^{-1}$). After quenched to room

temperature, they were reground and heated at 1250 °C for a further 12 hours in alumina boats inside the same muffle furnace. After re-milling under the same conditions described above, the powders were subsequently re-sintered for 6.5 hours each, in a tube furnace at 1350 °C; three samples with the nominal compositions: $Ba_6Sc_{0.75}In_{0.25}Nb_9O_{30}$, $Ba_6Sc_{0.5}In_{0.5}Nb_9O_{30}$ and $Ba_6Sc_{0.25}In_{0.75}Nb_9O_{30}$ were obtained.

Pellets of these three materials were prepared by uniaxial pressing the powders to 1-1.1 tonne in a 10 mm diameter stainless steel die, producing a pressure of around 125-140 MPa. The green bodies were sintered on platinum foil in alumina boats inside a tube furnace for 12 hours at the temperature of 1300 °C, as previously reported in Ref. 6; further, they were cooled down to room temperature (heating and cooling rates used were of 10 $K \cdot min^{-1}$) [6]. The obtained cylindrical pellets had diameters typically between 9.6 and 9.9 mm and > 92% of relative density (ρ_r); a precise description of the relative densities obtained after sintering, but also of the employed reaction temperatures, sintering temperatures and their corresponding times are presented in Table 1.

Table 1 Fabrication details of $Ba_6Sc_{1-x}In_xNb_9O_{30}$ (x = 0.25, 0.5, 0.75) ceramic powders and pellets, and relative densities of the resulting pellets used for electrical studies

Compound	***Reaction temperatures/°C and (Reaction time/h)***	***Sintering temperatures/°C***	***Relative density/%***
$Ba_6Sc_{0.75}In_{0.25}Nb_9O_{30}$	1250 °C (12 h) + 1250 °C (12 h) +1350 °C (6.5 h)	1350 °C (12 h)	92.43
$Ba_6Sc_{0.50}In_{0.50}Nb_9O_{30}$	1250 °C (12 h) + 1250 °C (12 h) +1350 °C (6.5 h)	1350 °C (12 h)	93.34
$Ba_6Sc_{0.25}In_{0.75}Nb_9O_{30}$	1250 °C (12 h) + 1250 °C (12 h) +1350 °C (6.5 h)	1350 °C (12 h)	92.87

2.2. Investigation techniques

In order to probe or distinguish between different regions within the ceramic, microstructural characterization techniques shall be used, while electrical measurements shall be performed in order to understand the behaviour within the electrically active microregions [39-42]. More commonly separation of grain boundary and bulk effects can be achieved by measuring electrical properties using techniques such as impedance spectroscopy [43]. For scanning electron microscopy (SEM) measurements, a JEOL JSM 5600 SEM with an EDX system, providing 3.5 nm resolution and a magnification of 300,000× was utilised. The employed current was ranging between 10^{-9} and 10^{-12} A, and the accelerating voltage from 0.5 to 30 kV. Small fragments of the ceramic pellets were placed on the carbon tape mounted on an alumminum specimen stub.

For the high-temperature impedance spectroscopy (HTIS) measurements, both planar external surfaces of the dense ceramic pellets were polished with SiC paper, then covered with organic-platinum paste electrodes (C2011004D5, Gwent Electronic Materials Ltd, UK). Each pellet face was covered with electrode paste were dried at 80 °C and placed on platinum foil and cured at 900 °C for approximately 1 hour in order to obtain Pt electrodes (eliminate the organic parts) and sinter the electrode. The electroded samples were mounted in an impedance alumina jig, similar to the one designed by Bruce and West [44]; the impedance jig was placed in a horizontal tube furnace controlled to ± 1 ºC. The temperature was increased step by step and when samples had reaching the desired temperature, they were left to equilibrate for approximately 15-20 minutes before taking the measurement. A Hewlett Packard 4192A LF impedance analyser was used to collect data over a frequency range of *ca.* 5 Hz – 13 MHz, in the temperature range *r.t.*–900 K and under an applied ac voltage of 100 mV. Data analysis was carried out using commercial "ZView" software, version 2.9c [45]; both complex plane plots and spectroscopic plots of both impedance and modulus formalisms were utilised [6,13]. The low-temperature dielectric spectroscopy (LTDS) measurements were performed on Agilent 4294 and HP 4192A impedance analysers in the frequency range of 5 Hz-10 MHz using an AC excitation of 500 mV, and in the temperature range between 50 and 350 K with the cooling rate of 2 $K \cdot min^{-1}$ using a closed system helium cryocooler with DE 202 cold head (A.S. Scientific products Ltd, UK) with a Sumitomo HC-2 compressor. Before starting the measurements, the samples were heated up to 350 K and kept isothermally in order to stabilise for approximately 15 mins; only afterwards, the dielectric spectroscopy data were collected on cooling [6,36].

3. Results and discussion

3.1 Structural results for the $Ba_6Sc_{1-x}In_xNb_9O_{30}$ (x = 0.25, 0.5, 0.75) ceramics

Room temperature powder X-ray diffraction (PXRD) patterns of $Ba_6Sc_{1-x}In_xNb_9O_{30}$ (x = 0.25, 0.5, 0.75) crushed pellets are presented in Figure 1. All three samples adopt the TTB structure with only small amount of $Ba_5Nb_4O_{15}$ slab perovskite secondary phase appearing at 31° (2θ); the amount of minor phase decreases with introducing more In (Figure 1).

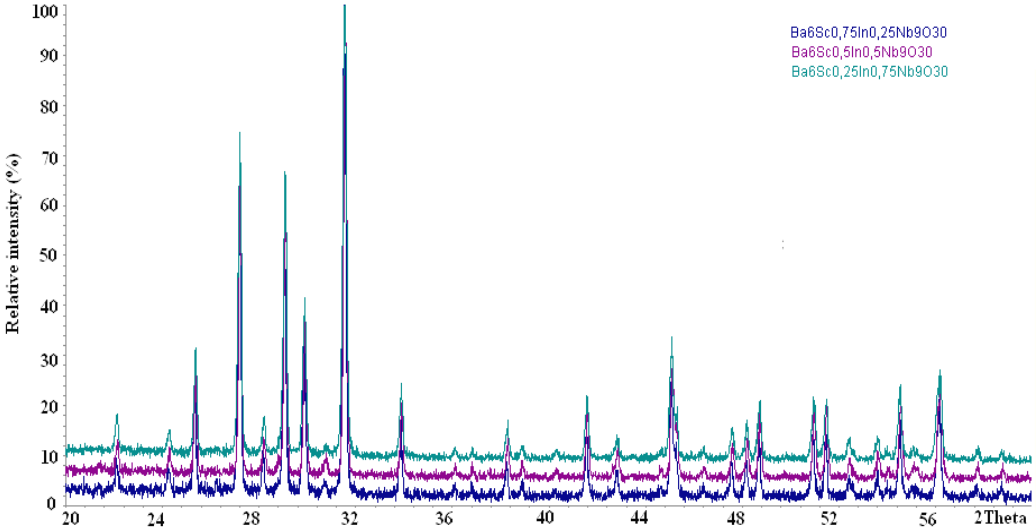

Figure 1 Room temperature powder X-ray diffraction data for $Ba_6Sc_{0.75}In_{0.25}Nb_9O_{30}$ (bottom), $Ba_6Sc_{0.5}In_{0.5}Nb_9O_{30}$ (middle) and $Ba_6Sc_{0.25}In_{0.75}Nb_9O_{30}$ (top); $Ba_5Nb_4O_{15}$ main peak at 31° (2θ).

All three were refined further in the space group *P4/mbm* (No. 127) using the Rietveld method [46], Figure 2, and the unit cell and goodness-of-fit parameters are presented in Table 2. Even if the amount of Sc/In is changing, the average radius of <Sc,In> changes only slightly from 0.665 Å to 0.755 Å (and diluted even more in the overall average B-site radius (Sc,In):Nb ratio of 1:9), therefore the lattice parameters corresponding to the three investigated compounds are very similar (Table 2).

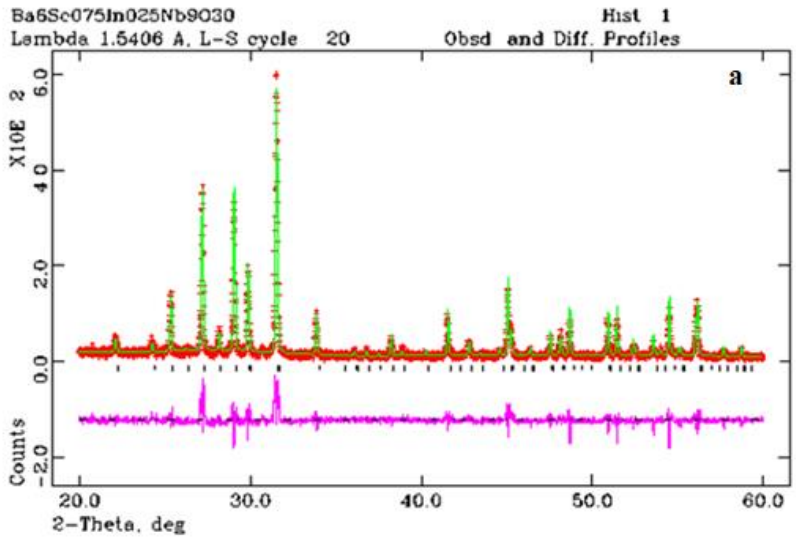

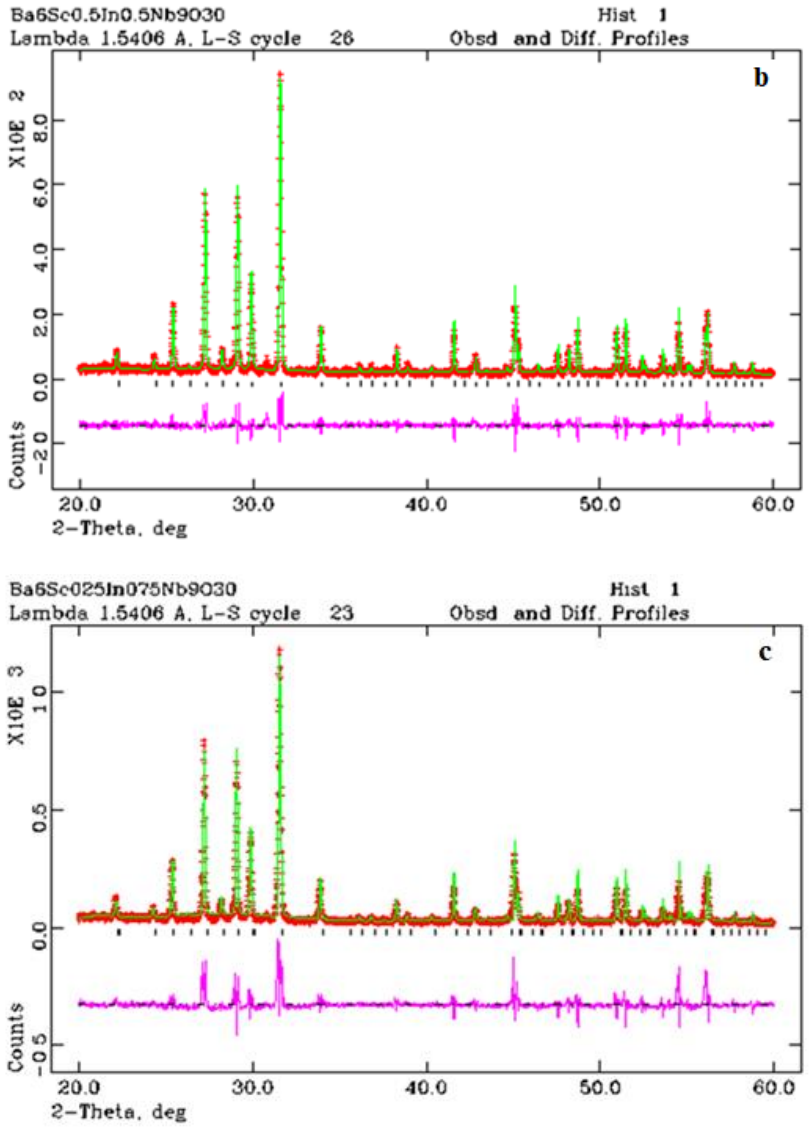

Figure 2 Rietveld refinement profiles of room temperature powder X-ray data in centrosymmetric, tetragonal space group *P4/mbm* for: $Ba_6Sc_{0.75}In_{0.25}Nb_9O_{30}$ (a); $Ba_6Sc_{0.50}In_{0.50}Nb_9O_{30}$ (b); and $Ba_6Sc_{0.25}In_{0.75}Nb_9O_{30}$ (c).

Table 2 Unit cell dimensions and goodness-of-fit parameters for $Ba_6Sc_{1-x}In_xNb_9O_{30}$ (x = 0.25, 0.5, 0.75) refined from XRD data in space group *P4/mbm*.

Compound	***a* (Å)**	***c* (Å)**	***V* (Å^3)**	R_p **(%)**	wR_p **(%)**	χ^2
$Ba_6Sc_{0.75}In_{0.25}Nb_9O_{30}$	12.66570(50)	4.02058(18)	644.984(25)	6.23	3.98	4.602
$Ba_6Sc_{0.50}In_{0.50}Nb_9O_{30}$	12.66070(40)	4.01964(14)	644.320(45)	5.98	5.37	5.28
$Ba_6Sc_{0.25}In_{0.75}Nb_9O_{30}$	12.66020(60)	4.02089(24)	644.471(40)	6.21	6.29	7.36

3.2 Microstructural analysis and high-temperature impedance spectroscopy

All investigated of the Sc-In solid solutions pellets were white, with no evident colour gradient on the external or fracture surfaces. Representative SEM micrographs of the ceramic microstructures are shown in Figure 3.

Micrographs of the three Sc-In solid solutions reveal a highly dense microstructure with well-bonded grains. The parallelepiped/columnar nature of the grains can be observed; the grain size appears to be fairly uniform and of the order of 4-6 μm long and 2-3 μm wide (*i.e.*, Figure 3a).

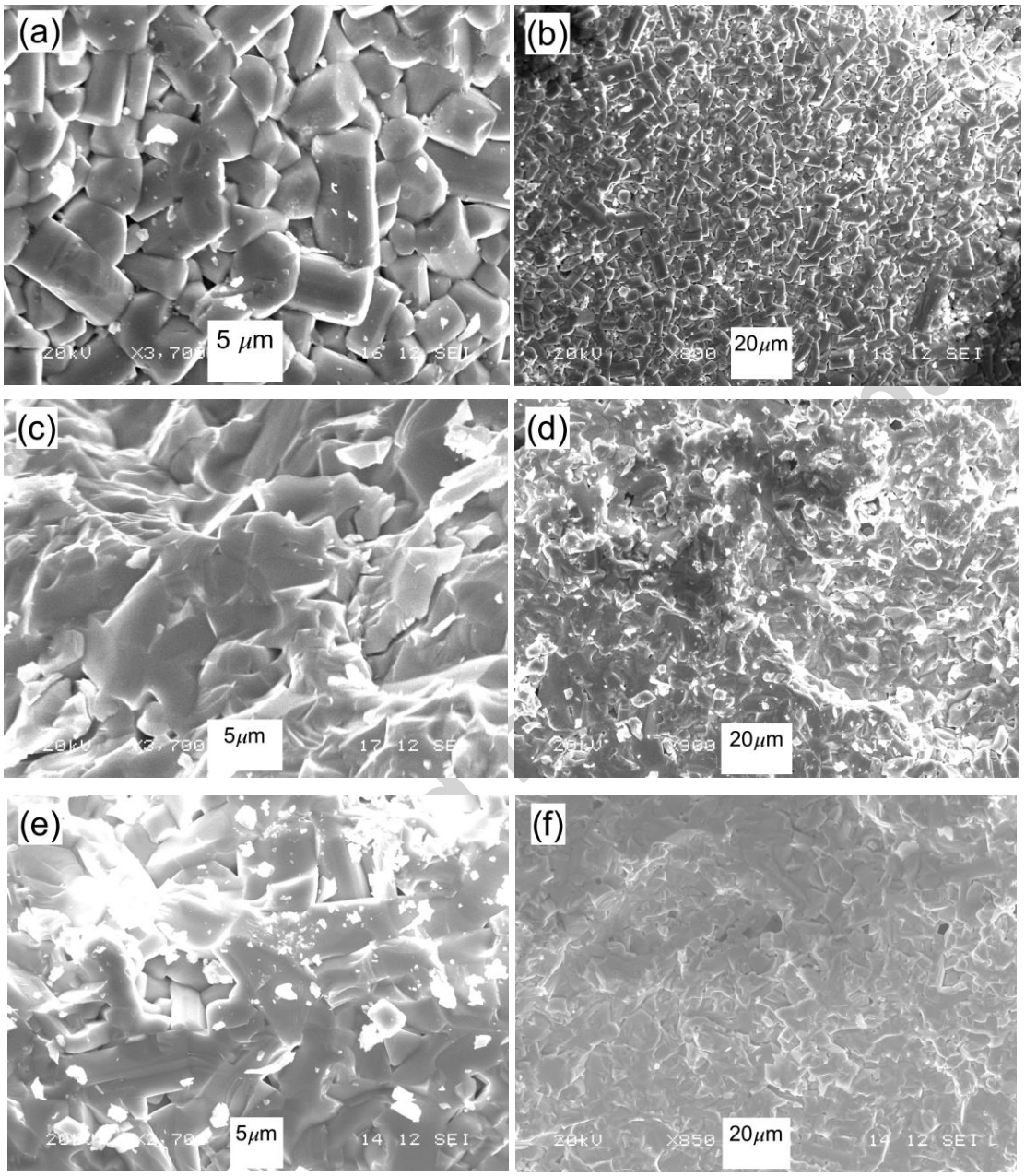

Figure 3 SEM images of the fracture surface of $Ba_6Sc_{0.75}In_{0.25}Nb_9O_{30}$ (a,b), $Ba_6Sc_{0.5}In_{0.5}Nb_9O_{30}$ (c,d) and $Ba_6Sc_{0.25}In_{0.75}Nb_9O_{30}$ (e,f) pellets sintered at 1350 °C.

Comparing these images to SEM images of $Ba_6ScNb_9O_{30}$ pellet prepared in the same conditions from Ref. 13, which have revealed a poor microstructure with poorly-bonded small-sized grains and significant continuous porosity, the microstructure of Sc-In solid solutions is much improved with enriching In content (Figures 3c and 3e). With increasing the

In content, the porosity becomes practically insignificant (Figures 3b, 3d and 3f), the grain boundaries appear less distinct and the resulting morphology resembles the $Ba_6InNb_9O_{30}$ sample reported previously [13].

In order to describe the electrical behaviour of different regions within the ceramics, high-temperature impedance spectroscopy (HTIS) was carried out as described previously in a similar work [13]. For the $Ba_6Sc_{1-x}In_xNb_9O_{30}$ system, the HTIS data are similar to those of Ga, Sc & In analogues of $Ba_6MNb_9O_{30}$, presented in Figures 6-8 of Ref. 13, therefore they are not presented here. Essentially, the spectra are dominated by a single response, as indicated by the appearance of a single Debye-like peak in both *M"* and *Z"* at the same characteristic relaxation frequency (f_{max}) – where *M"* stands for the imaginary electric modulus and *Z"* represents the imaginary impedance. From the magnitude of associated capacitance (~ 10^{-11} F), this is attributed to the bulk response. In all samples, the *Z"* peak shows some asymmetry in the lower frequency side and suggests a minor grain boundary contribution, but it is not possible to resolve this sufficiently to extract associated R and C values [47].

Bulk conductivities (σ_b) and relaxation times (τ_b) were extracted from *M"* spectra as described in Ref. 13 and are shown in Arrhenius format in Figures 4 and 5. The data correspond well to that reported for Sc and In analogues [13]. The Sc-In solid solutions samples exhibit similar behaviour to the Sc compound and again, the In sample has a slightly different activation energy, Table 3.

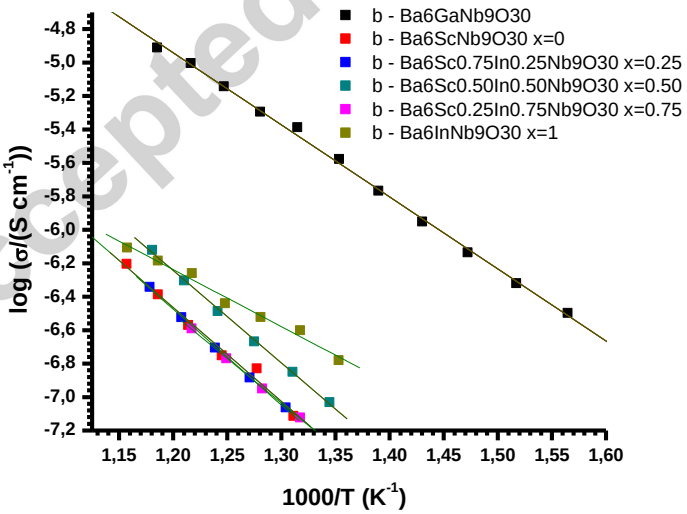

Figure 4 Arrhenius plot of the bulk electrical conductivity data (from $M"_{max}$ *vs.* freq.) for $Ba_6Sc_{1-x}In_xNb_9O_{30}$ (x = 0.25, 0.5, 0.75) in comparison with $Ba_6MNb_9O_{30}$ (M = Ga, Sc, In) [13].

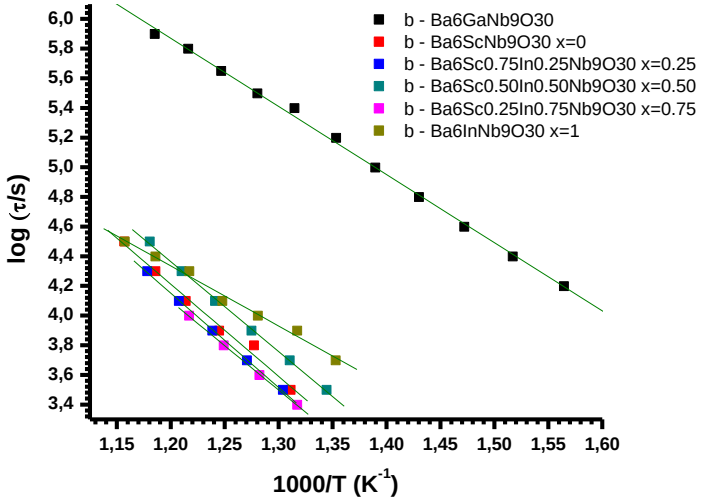

Figure 5 Arrhenius plots of the bulk time constant data (from M''_{max} *vs.* freq.) for $Ba_6Sc_{1-x}In_xNb_9O_{30}$ (x = 0.25, 0.5, 0.75) in comparison with $Ba_6MNb_9O_{30}$ (M = Ga, Sc, In) [13].

Generally, a small decrease of the activation energy is observed when decreasing the Sc content for the conduction process (Table 3). The same analysis was also carried out using *Z''* data and gave good agreement, Table 3, with the exception of the In analogue which had significantly different E_a values as determined from the *M''* and *Z''* spectra; this difference is due to the influence of the grain boundary resistance contributing the *Z''* data, but not affecting the capacitive response (*M''* data). The reason for the significantly different E_a value for the In composition is not clear.

Table 3 Bulk activation energies for $Ba_6Sc_{1-x}In_xNb_9O_{30}$ (x = 0.25, 0.5, 0.75) electrical conduction processes; data extracted from the electrical conductivity (σ) and time constant (τ). Comparison with $Ba_6Sc_{1-x}In_xNb_9O_{30}$ (x = 1, 0) [13].

Compound	σ_{bulk}		τ_{bulk}	
	(M'' data)	***(Z'' data)***	***(M'' data)***	***(Z'' data)***
$Ba_6ScNb_9O_{30}$	E_a=**1.114**±0.083 r=0.99272	E_a=**1.127**±0.031 r=0.99810	E_a=**1.233**±0.065 r=0.99440	E_a=**1.262**±0.028 r=0.99877
$Ba_6Sc_{0.75}In_{0.25}Nb_9O_{30}$	E_a=**1.137**±0.018 r=0.99959	E_a=**1.196**±0.014 r=0.99985	E_a=**1.261**±0.018 r=0.99970	E_a=**1.484**±0.093 r=0.99606
$Ba_6Sc_{0.50}In_{0.50}Nb_9O_{30}$	E_a=**1.095**±0.020 r=0.99937	E_a=**1.108**±0.012 r=0.99975	E_a=**1.203**±0.020 r=0.99942	E_a=**1.203**±0.020 r=0.99942
$Ba_6Sc_{0.25}In_{0.75}Nb_9O_{30}$	E_a=**1.057**±0.022 r=0.99957	-*	E_a=**1.188**±0.018 r=0.99977	-*
$Ba_6InNb_9O_{30}$	E_a=**0.676**±0.036 r=0.99287	E_a=**0.820**±0.047 r=0.99181	E_a=**0.803**±0.036 r=0.99498	E_a=**1.238**±0.059 r=0.99435

r - correlation coefficient; E_a - activation energy (eV); *only two data points available

3.3 Low-temperature dielectric spectroscopy and Vogel-Fulcher analysis

Dielectric spectroscopy data in the range 50 to 350 K showed that all three compounds exhibit characteristic relaxor behaviour with a strong frequency dependence of peaks in both dielectric constant and dielectric loss as a function of temperature (Figures 6, 7 and 8); these results are consistent with those obtained in Ref. 13. The dielectric curves are displaced to higher temperatures with increasing average B-site ionic radius (increasing x), due to expansion of the crystal lattice (Vegard's Law). This expansion is anisotropic with the c-axis expanding greater relative to the ab plane; this increases the tetragonality (*c/a*) which stabilizes the polar ordering to higher temperatures [9-13]. The experimental measuring setup was programmed to acquire data very fast for each frequency at a certain temperature, while the samples were subjected to a controlled linear non-isothermal regime, in order to further characterise the relaxor behaviour with higher temperature and frequency resolution.

Dielectric data for $Ba_6Sc_{0.75}In_{0.25}Nb_9O_{30}$, are shown in Figure 6. The dielectric permittivity (Figure 6a) decreases with increasing frequency and its corresponding maxima shifts towards higher temperatures (T_m). The dielectric loss is also frequency-dependent, but the curve maxima are shifted to higher temperature relative to the dielectric permittivity; for the same frequency, the temperature of the dielectric loss maximum, T_m, has a different value than the dielectric permittivity one. The dielectric loss maximum shifts towards higher temperatures with increasing frequency (Figure 6b). At high temperatures, and most commonly above T_m, the dielectric loss increases with increasing frequency; at lowest temperatures, the dielectric loss decreases with increasing frequency. Dielectric data for the $Ba_6Sc_{0.5}In_{0.5}Nb_9O_{30}$ and $Ba_6Sc_{0.25}In_{0.75}Nb_9O_{30}$ ceramics are shown in Figures 7 and 8, respectively. They exhibit the same trends as $Ba_6Sc_{0.75}In_{0.25}Nb_9O_{30}$, but shifted to higher temperatures for the same corresponding frequencies.

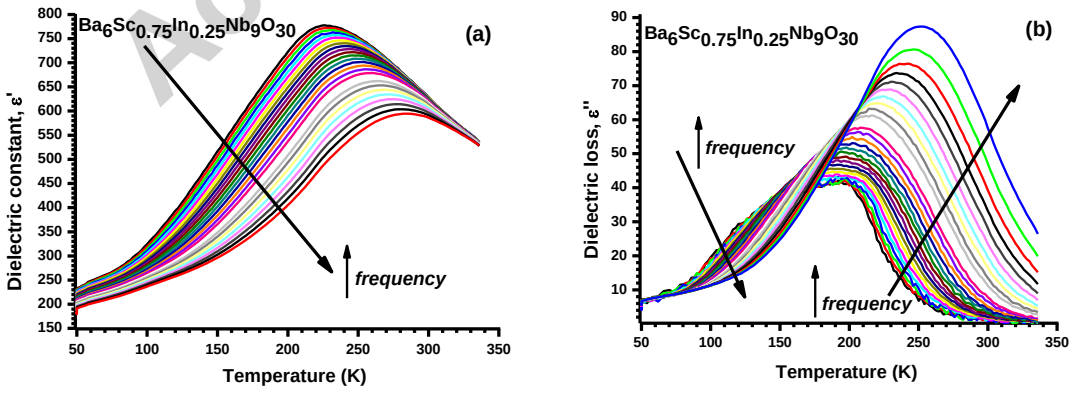

Figure 6 Dielectric constant (a) and loss (b) as a function of frequency and temperature for $Ba_6Sc_{0.75}In_{0.25}Nb_9O_{30}$.

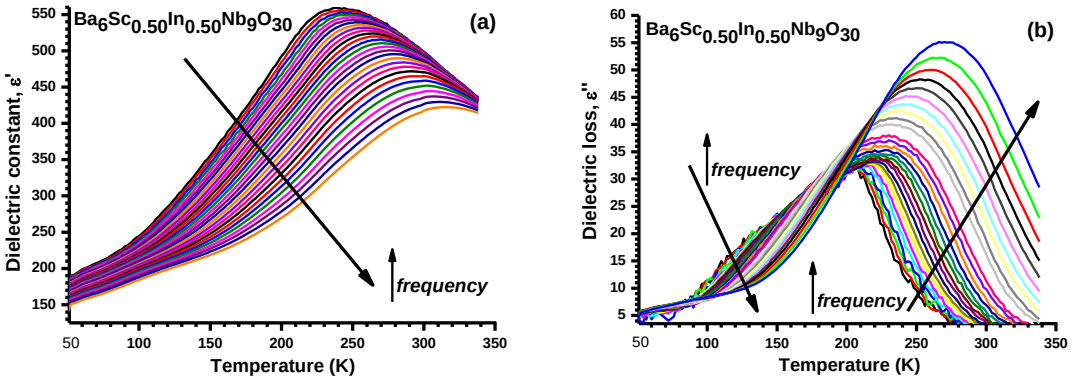

Figure 7 Dielectric constant (a) and loss (b) as a function of frequency and temperature for $Ba_6Sc_{0.5}In_{0.5}Nb_9O_{30}$.

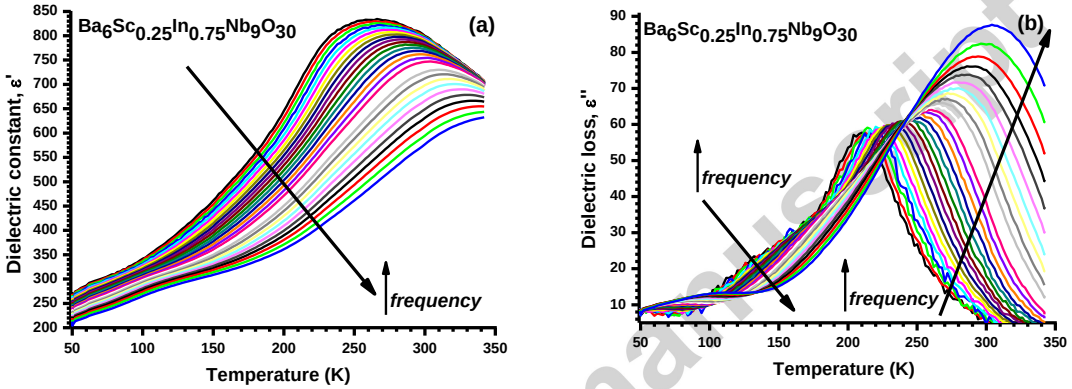

Figure 8 Dielectric constant (a) and loss (b) as a function of frequency and temperature for $Ba_6Sc_{0.25}In_{0.75}Nb_9O_{30}$.

For comparative purposes the dielectric permittivity of the three investigated compounds are presented in Figure 9 together with those of $Ba_6ScNb_9O_{30}$ and $Ba_6InNb_9O_{30}$, at the same frequencies of f = 1.467 kHz (Figure 9a), f = 6.812 kHz (Figure 9b) and f = 1 MHz (Figure 9c). In each case the dielectric permittivity curves (and therefore T_m values) are shifted to higher temperatures with increasing In content. With increasing In the peaks also become more asymmetric and the curves flatten at temperatures above T_m.

There is no sustained trend of the magnitude of dielectric permittivity maxima with changing composition within the Sc-In solid solutions, but this is probably due to microstructural differences as a result of differences between the optimum and the actual processing temperature (1350 °C).

In all compounds the dielectric loss curves (and to a lesser extent also in the dielectric permittivity ones), a second response appears on the low temperature side of the peak

maxima; this additional feature becomes more evident with increasing In content – Figures 6b, 7b and 8b. At the highest In concentrations, another small peak in the dielectric permittivity may be observed between roughly 60 and 180 K (Figure 9). This additional (third) process becomes more relevant with increasing the frequency (Figure 9c).

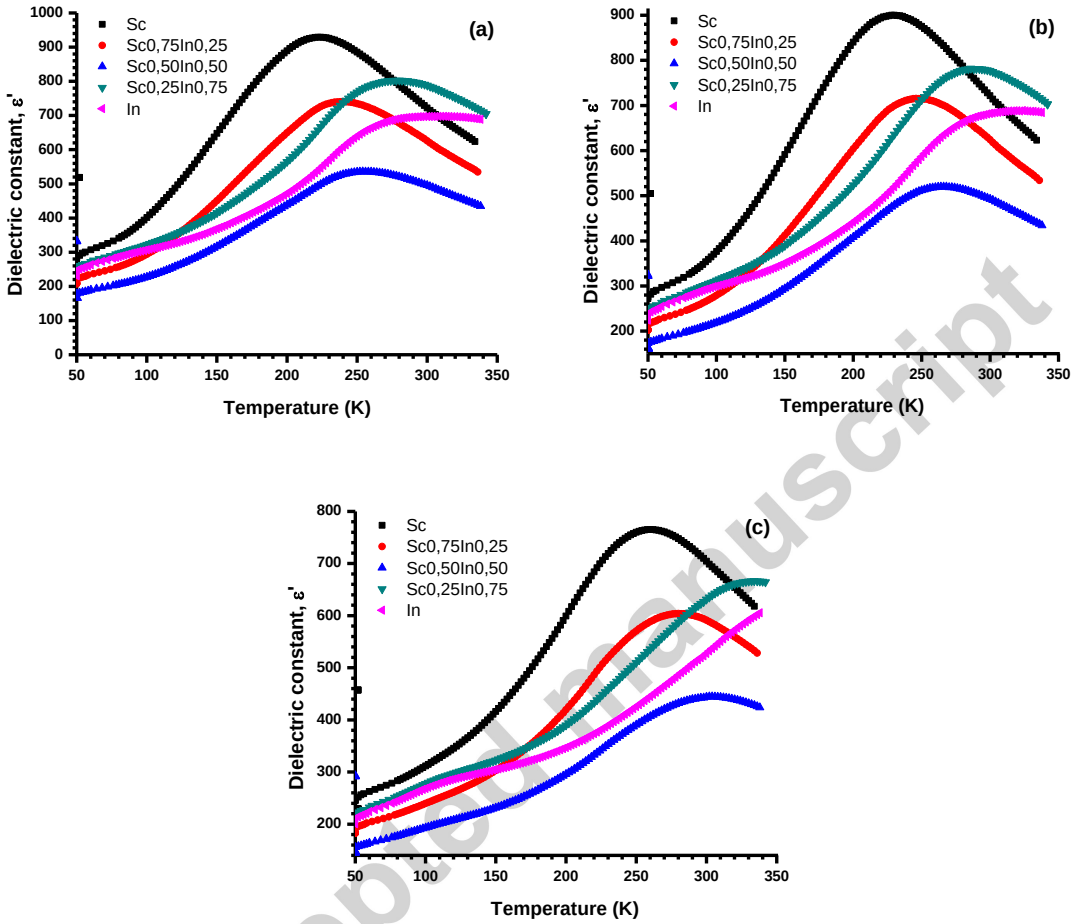

Figure 9 Dielectric constant of $Ba_6Sc_{1-x}In_xNb_9O_{30}$ (x = 0.25, 0.5, 0.75) ceramics in comparison with the $Ba_6Sc_{1-x}In_xNb_9O_{30}$ (x = 1, 0) ceramics [13], as a function of temperature for the frequencies of 1.467 kHz (a), 6.812 kHz (b) and 1 MHz (c).

The analysis of the dielectric relaxation processes in $Ba_6Sc_{1-x}In_xNb_9O_{30}$ (x = 0.25, 0.5, 0.75) ceramics is performed in the first stage by fitting the dielectric permittivity data with the Vogel-Fulcher model [48,49]. From the Vogel-Fulcher (VF) curves, Figure 10, it clear once again that with increasing the ionic radius of the B-site species (replacing Sc with In), the curves are displaced to higher temperature and that relaxor degree increases as denoted by the increased T_m range (curvature of plots). It is also important to note that for the Sc-In

intermediates, the VF curves are not smoothly curved but appear rather linear over certain regions [6].

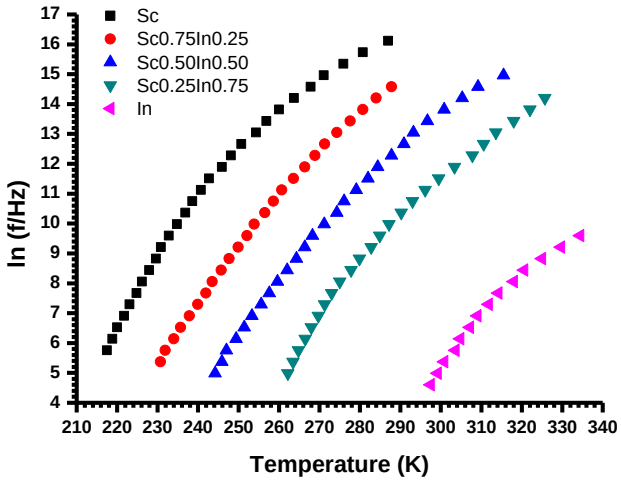

Figure 10 Vogel-Fulcher representation of the dielectric permitivity data for solid solution samples $Ba_6Sc_{1-x}In_xNb_9O_{30}$ (x = 0.25, 0.5, 0.75), compared with Sc and In end-members [12,36].

As Sc is replaced with In, and the VF curves are shifted towards higher temperatures, the possibility of obtaining T_m values at low frequencies increases as discussed previously. Also, the second process that becomes apparent (particularly in the dielectric loss data) is not well separated from the main relaxation process and thus it influences the main peak and therefore the VF curves in Figure 10. The VF curves for the Sc-In samples, where some regions appear to deviate from their expected curvature, might be due to these additional relaxation processes that interfere with the main one. When increasing the In content, the flattening of the ε' peaks at high frequencies, and also their shift beyond the temperature measuring window, make the acquisition of data in this important region much more difficult.

Vogel-Fulcher free-fits of $T_m(f)$ extracted from dielectric permittivity data for $Ba_6Sc_{1-x}In_xNb_9O_{30}$ (x = 0.25, 0.5, 0.75) ceramics are presented in Figures 11a-c; the resulting VF parameters are presented in Table 4.

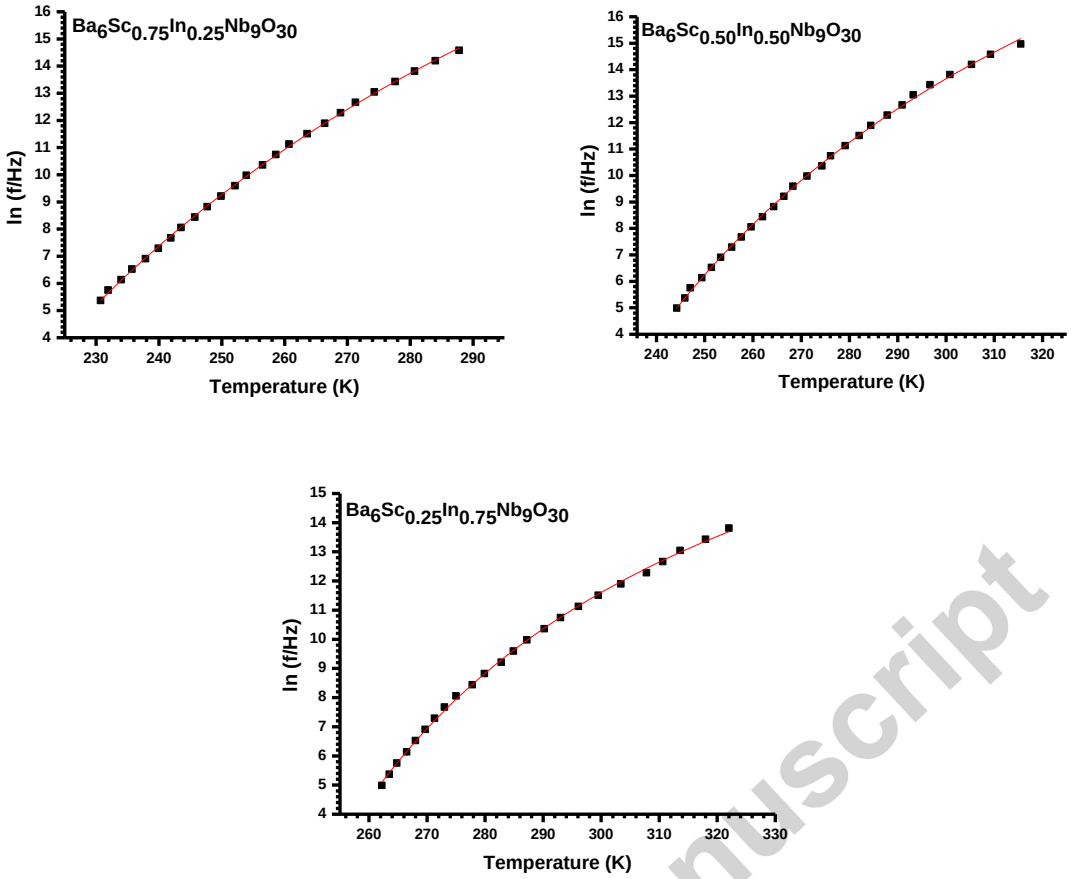

Figure 11 Vogel-Fulcher free-fits of $T_m(f)$ extracted from dielectric constant data for $Ba_6Sc_{0.75}In_{0.25}Nb_9O_{30}$ (a), $Ba_6Sc_{0.5}In_{0.5}Nb_9O_{30}$ (b) and $Ba_6Sc_{0.25}In_{0.75}Nb_9O_{30}$ (c).

Table 4 Vogel-Fulcher and goodness-of-fit parameters for $Ba_6Sc_{1-x}In_xNb_9O_{30}$ (x = 0.25, 0.5, 0.75) ceramics, determined from data fitting in Figure 11. Data for Sc and In end-members are provided for comparison [13].

Compound	T_{VF} ***(K)***	f_0 ***(Hz)***	**ln(f_0/Hz)**	E_a ***(eV)***	χ^2
$Ba_6ScNb_9O_{30}$	154.07 ± 1.49	$1.66 \times 10^{11} \pm 3$	25.83 ± 0.26	0.1101 ± 0.0038	0.05558
$Ba_6Sc_{0.75}In_{0.25}Nb_9O_{30}$	91.53 ± 6.50	$1.60 \times 10^{16} \pm 3$	37.31 ± 1.09	0.3829 ± 0.0308	0.05167
$Ba_6Sc_{0.50}In_{0.50}Nb_9O_{30}$	122.41 ± 6.02	$1.39 \times 10^{14} \pm 2$	32.57 ± 0.91	0.2894 ± 0.0236	0.07739
$Ba_6Sc_{0.25}In_{0.75}Nb_9O_{30}$	188.95 ± 3.46	$3.31 \times 10^{10} \pm 1$	24.22 ± 0.54	0.1207 ± 0.0090	0.07530
$Ba_6InNb_9O_{30}$	253.06 ± 3.52	$6.50 \times 10^{6} \pm 2$	15.69 ± 0.54	0.0425 ± 0.0054	0.06277

As can be seen form Table 4, data do not demonstrate any systematic variation that might be expected for solid solutions. The variation of f_0 in particular is a cause for concern, with values ranging over ten orders of magnitude. Clearly this is not easily explained by minor changes in composition.

The results so far forecast an uncertain procedure to analyse the dielectric permittivity data and obtain correct values for characterising the relaxation processes. The peak asymmetry (especially in the dielectric loss data) advocate in-depth analyses of the dielectric

loss curves by employing other methodologies for characterising the relaxation processes such as the universal dielectric response (UDR) model [50-52]. In addition, the processing of the materials – which might induce subtle structural and microstructural changes and so introduce additional dielectric processes [6], affect the Vogel-Fulcher evaluation of data [6,12,36]. These aspects will be investigated in greater detail in a following paper.

4. Conclusions

In this article, the structural, microstructural, electrical and relaxor properties of the Sc-In solid solutions within the $Ba_6Sc_{1-x}In_xNb_9O_{30}$ (x = 0-1) system were investigated. For the electrical behaviour of different regions, high-temperature impedance spectroscopy of the intermediate compounds revealed similar results to those of Ga, Sc and In analogues; the complex immitance (M^* and Z^*) spectra are dominated by a single response (appearance of a single Debye-like peak in both M'' and Z'' with coinciding, characteristic f_{max}), and which was attributed to the bulk response. The subtle asymmetry of the Z" peak suggested a minor contribution of the grain boundary response. The Sc-In solid solutions samples exhibit similar electrical behaviour especially to the Sc compound, while the In sample has a slightly different activation energy (significantly different E_a values as determined from the M'' and Z'' spectra - this difference is due to the influence of the grain boundary resistance contributing the Z'' data, but not affecting the capacitive response – M'' data); a small decrease of the activation energy is observed when decreasing the Sc content for the conduction process.

For the dielectric spectroscopy measurements at lower temperature, the permittivity and loss curves (and therefore the T_m values) are shifted to higher temperatures with increasing the average ionic radius of <Sc,In> on the B-site. With increasing the content of In, the peaks also become more asymmetric and the curves flatten more at temperatures above T_m, but there is however no sustained trend for the magnitudes of their maxima. Also, the in-depth analysis of the relaxor behaviour was carried out. The step-wise increase of the ionic radius of the M cation on the B-site led to the displacement at higher temperature of the Vogel-Fulcher (VF) curves, and as denoted by the increased T_m range of the ln$f$ *vs.* T_m curvature it resulted in an increase in the degree of relaxor behaviour. However, the dipole freezing temperature, T_{VF}, determined by Vogel-Fulcher model does not simply increases linearly as a function of M cation size. Moreover, the extrapolation of VF-like curves results in considerably different values when compared to those found in the previous papers [12,36,13], since the acquired dielectric data seem to be very sensitive to preparative

conditions. The investigation of the dielectric relaxation processes, with respect to the reproducibility and validity of the results, has revealed some uncertainties produced by using the Vogel-Fulcher equation for fitting the dielectric permittivity data: the physical results are severely influenced by sample processing.

Acknowledgements:

The authors would like to thank to the following funding organisations: the Royal Society for providing a research fellowship (F.D.M.), EPSRC for providing the PhD student grant (A.R.) and Roberto Rocca Education Program for providing an additional fellowship grant (A.R.).

References

[1] Jindal, S.; Vasishth A.; Devi, S.; Anand, G. A review on tungsten bronze ferroelectric ceramics as electrically tunable devices. *Integrated Ferroelectrics*, **2018**;186(1),1-9.

[2] Yang, B.; Hao, S.; Yang, P.; Wei, L.; Yang, Z. Relaxor behavior and energy storage density induced by B-sites substitutions in $(Ca_{0.28}Ba_{0.72})_{2.1}Na_{0.8}Nb_5O_{15}$ Tungsten bronze ceramics. *Ceram. Int.* **2018**, 44 (8), 8832-8841.

[3] Thummavichai, K.; Xia,Y.; Zhu, Y. Recent progress in chromogenic research of tungsten oxides towards energy-related applications. *Progress Mater. Sci*. **2017**, 88, 281-324.

[4] Shimizu K.; Kato H.; Kobayashi M.; Kakihana, M. Synthesis and photocatalytic properties of tetragonal tungsten bronze type oxynitrides. *Appl. Catal. B: Environm.* **2017**, 206, 444-448.

[5] Botella, P.; Solsona, B.; Garcia-Gonzalez, E.; Gonzalez-Calbet, J.M.; Lopez Nieto, J.M. The hydrothermal synthesis of tetragonal tungsten bronze-based catalysts for the selective oxidation of hydrocarbons. *Chem. Comm.* **2007**, 0, 5040–5042.

[6] Rotaru, A. *PhD Thesis*, University of St Andrews, **2013**.

[7] Villafuerte-Castrejon, M.E.; Moran, E.; Reyes-Montero, A.; Vivar-Ocampo, R.; Pena-Jimenez, J-.A.; Rea-Lopez, S.-O.; Pardo, L. Towards Lead-Free Piezoceramics: Facing a Synthesis Challenge. *Materials* **2015**, 9, 21.

[8] Zu, X.; Fu, M.; Stennett, M.C.; Villarinho, P.M.; Levin, I.; Randall, C.A.; Gardner, J.; Morrison, F.D.; Reaney, I.M. A Crystal-Chemical Framework for Relaxor versus Normal Ferroelectric Behavior in Tetragonal Tungsten Bronzes. *Chem. Matter.* **2015**, 27, 3250–3261.

[9] Arnold, D.C.; Morrison, F.D. B-cation effects in relaxor and ferroelectric tetragonal tungsten bronzes. *J. Mater. Chem.* **2009**, 19, 6485-6488.

[10] Rotaru, A.; Miller, A.J.; Arnold, D.C.; Morrison, F.D. Towards novel multiferroic & magnetoelectric materials: dipole stability in tetragonal tungsten bronzes. *Phil. Trans. Royal Soc. A: Math. Phys. Eng. Sci.* **2014**, 372, 20120451.

[11] Gardner, J.; Morrison, F.D. A-site size effect in a family of unfilled ferroelectric tetragonal tungsten bronzes: $Ba_4R_{0.67}Nb_{10}O_{30}$ (R = La, Nd, Sm, Gd, Dy and Y). *Dalton Trans.* **2014**, 43, 11687-11695.

[12] Rotaru, A.; Arnold, D.C.; Daoud-Aladine, A.; Morrison, F.D. Origin and stability of the dipolar response in a family of tetragonal tungsten bronze relaxors. *Phys. Rev. B.* **2011**, 83, 184302.

[13] Rotaru, A.; Morrison, F.D. Microstructural and high-temperature impedance spectroscopy study of $Ba_6MNb_9O_{30}$ (M = Ga, Sc, In) relaxor dielectric ceramics with tetragonal tungsten bronze structure. *Ceram. Int.* **2016**, 42, 11810-11821.

[14] Qu, W.; Tan, X.; McCallum, R.W.; Cann, D.P.; Ustundag, E. Room temperature magnetoelectric multiferroism through cation ordering in complex perovskite solid solutions. *J. Phys.: Cond. Matter* **2006**, 18, 8935.

[15] Simon, A.; Ravez, J. Solid-state chemistry and non-linear properties of tetragonal tungsten bronzes materials. *C. R. Chimie*, **2006**, 9, 1268-1276.

[16] Stennett, M.C.; Miles, G.C.; Sharman, J.; Reaney, I.M.; West, A.R. A new family of ferroelectric tetragonal tungsten bronze phases, $Ba_2MTi_2X_3O_{15}$. *J. Eur. Ceram. Soc.* **2005**, 25, 2471-2475.

[17] Stennett, M.C.; Reaney, I.M.; Miles, G.C.; Woodward, D.I.; West, A.R.; Kirk, C.A.; Levin, I. Dielectric and structural studies of $Ba_2MTi_2Nb_3O_{15}$ ($BMTNO_{15}$, M= Bi^{3+}, La^{3+}, Nd^{3+}, Sm^{3+}, Gd^{3+}) tetragonal tungsten bronze-structured ceramics. *J. Appl. Phys.* **2007**, 101, 4114.

[18] Chen, X.M.; Yang, J.S. Dielectric characteristics of ceramics in $BaO–Nd_2O_3–TiO_2–Ta_2O_5$ system. *J. Eur. Ceram. Soc.* **1999**, 19, 139-142.

[19] Chen, X.M.; Liu, C.L.; Yang, J.S.; Wu, Y.J. Some Tungsten–Bronze Compounds in the $BaO–Nd_2O_3–TiO_2–Ta_2O_5$ System. *J. Solid State Chem.* **1999**, 148, 438-441.

[20] P.R.; Irvine, J.T.S. Synthesis and electrical characterisation of the tetragonal tungsten bronze type phases,$(Ba/Sr/Ca/La)_{0.6}M_xNb_{1-x}O_{3-\delta}$ (M= Mg, Ni, Mn, Cr, Fe, In, Sn): evaluation as potential anode materials for solid oxide fuel cells. *Solid State Ionics* **1999**, 124, 61-72.

[21] Miller, A.J.; Rotaru, A.; Arnold, D.C.; Morrison F.D. Effect of local A-strain on dipole stability in $A_6GaNb_9O_{30}$ (A = Ba, Sr, Ca) tetragonal tungsten bronze relaxor dielectrics. *Dalton Trans.* **2015**, 44, 10738-10745.

[22] Castel E.; Josse, M.; Michau, D.; Maglione, M. Flexible relaxor materials: $Ba_2Pr_xNd_{1-x}FeNb_4O_{15}$ tetragonal tungsten bronze solid solution. *J Phys: Condens Matter.* **2009**, 21, 452201.

[23] Josse, M.; Bidault, O.; Roulland, F.; Castel, E.; Simon, A.; Michau, D.; Von der Muhll, R.; Nguyen, O.; Maglione, M. The $Ba_2LnFeNb_4O_{15}$"tetragonal tungsten bronze": Towards RT composite multiferroics. *Solid State Sci.* **2009**, 11,1118-11123.

[24] Castel, E.; Josse, M.; Roulland, F.; Michau, D.; Raison, L.; Maglione, M. In-situ formation of barium ferrite in iron-doped "tetragonal tungsten bronze": Elaboration of room temperature multiferroic composites. *J. Magn. Magn. Mater.* **2009**, 321, 1773-1777.

[25] Albino, M.; Veber, P.; Pechev, S.; Labrugere, C.; Velazquez, M.; Maglione, M.; Josse, M. Growth and Characterization of $Ba_2LnFeNb_4O_{15}$ (Ln = Pr, Nd, Sm, Eu) Relaxor Single Crystals. *Cryst Growth Design.* **2014**, 14, 500-12.

[26] Roulland, F.; Josse, M.; Castel, E.; Maglione, M. Influence of ceramic process and Eu content on the composite multiferroic properties of the $Ba_{6-2x}Ln_{2x}Fe_{1+x}Nb_{9-x}O_{30}$ TTB system, *Solid State Sci.* **2009**, 11, 1709–1716.

[27] Lines, M.E.; Glass, A.M. *Principles and applications of ferroelectrics and related materials*, Oxford University Press, **2001**.

[28] McCabe, E.E.; West, A.R. New high permittivity tetragonal tungsten bronze dielectrics $Ba_2LaMNb_4O_{15}$: M=Mn, Fe. *J. Solid State Chem.* **2010**, 183, 624–630.

[29] Brandt, R.; Muller-Buschbaum, H. Zur Kristallchemie der tetragonalen Wolframbronze: $Ba_6FeNb_9O_{30}$. *Monats. Chem.* **1986**, 117, 1239-1244.

[30] Henshaw, G.S.; Gellman, L.J.; Williams, D.E. Selectivity and composition dependence of response of gas-sensitive resistors. Part 1.—Propane–carbon monoxide selectivity of $Ba_6Fe_xNb_{10-x}O_{30}$ ($1 \leqslant x \leqslant 2$). *J. Mater. Chem.* **1994**, 4, 1427-1431.

[31] Krainik, N.N.; Isupov, V.A.; Bryzhina, M.F.; Agranovskaya, A.I. Crystal chemistry of ferroelectrics with structural type of tetragonal oxygen tungsten bronze. *Soviet Physics – Crystallography* **1964**, 9, 281.

[32] Damjanovic, D. Ferroelectric, dielectric and piezoelectric properties of ferroelectric thin films and ceramics. *Rep. Prog. Phys.*, **1998**, 61, 1267.

[33] Hirota, K.; Wakimoto, S.; Cox, D.E. Neutron and x-ray scattering studies of relaxors. *J. Phys. Soc. Jpn.* **2006**, 75, 111006.

[34] Jeong, D.Y. *PhD Thesis*, The Pennsylvania State University, **2004**.

[35] Shvartsman, V.V.; Lupascu, D.C. Lead-Free Relaxor Ferroelectrics. *J. Am. Ceram. Soc.* **2012**, 95, 1-26.

[36] Rotaru, A.; Morrison, F.D. Vogel-Fulcher analysis of relaxor dielectrics with the tetragonal tungsten bronze structure $Ba_6MNb_9O_{30}$ (M = Ga, Sc, In). *J. Therm. Anal. Calorim.* **2015**, 120, 1249-1259.

[37] Rotaru, A.; Schiemer J.A.; Carpenter, M.A. Elastic and anelastic relaxations accompanying relaxor dielectric behaviour of $Ba_6GaNb_9O_{30}$ tetragonal tungsten bronze from resonant ultrasound spectroscopy. *J. Therm. Anal. Calorim.* **2016**, 124, 571-583.

[38] Rotaru, A. *First year report of the PhD Thesis*, University of St Andrews, **2008**.

[39] Guo, Z.; Zhu, Q.; Wu, S.; Hu, C.; Liu, L.;, Fang L. Effect of annealing atmosphere on the structure and dielectric properties of unfilled tungsten bronze ceramics $Ba_4PrFe_{0.5}Nb_{9.5}O_{30}$. *Ceram. Int.* **2018**, 44(7), 7700-7708.

[40] Lalena, J.N.; Cleary, D.A. *Principles of Inorganic Materials Design*, John Wiley & Sons Inc., Hoboken, New Jersey, **2005**.

[41] Irvine, J.T.S.; Sinclair, D.C.; West, A.R. Electroceramics: characterization by impedance spectroscopy. *Adv. Mater.* **1990**, 2, 132-138.

[42] Pradhan, D.K.; Behera, B.; Das, P.R. Studies of dielectric and electrical properties of a new type of complex tungsten bronze electroceramics. *J. Mater. Sci.: Mater. Electron.* **2012**, 23, 779–785.

[43] Hirose N.; West, A.R. Impedance spectroscopy of undoped $BaTiO_3$ ceramics. *J. Am. Ceram. Soc.*, **1996**, 79, 1633-1641.

[44] Bruce, P.G.; West, A.R. The A-C Conductivity of Polycrystalline LISICON, $Li_{2+2x}Zn_{1-x}GeO_4$, and a Model for Intergranular Constriction Resistances. *J. Electrochem. Soc.* **1983**, 130, 662-669.

[45] Johnson, D. Scribner Associates, Inc., **1995-2000**.

[46] Rietveld, H.M. A profile refinement method for nuclear and magnetic structures. *J. Appl. Cryst.*, 2 (**1969**) 65.

[47] Hodge, I.M.; Ingram, M.D.; West, A.R. Impedance and modulus spectroscopy of polycrystalline solid electrolytes. *J. Electroanal. Chem.* **1976**, 74, 125-143

[48] Vogel H. Das temperaturabhängigkeitsgesetz der viskosität von flüssigkeiten. *Phys Z.*, **1921**;22:645-6.

[49] Fulcher G.S. Analysis of recent measurements of the viscosity of glasses. *J Am Ceram Soc.* **1925**;8:339-55.

[50] Jonscher A.K., *Dielectric Relaxation in solids*, Chelsea Dielectrics Press, London, **1983**.

[51] Tagantsev A.K., Vogel-Fulcher relationship for the dielectric permittivity of relaxor ferroelectrics, *Phys. Rev. Lett.*, **1994**;72:1100.

[52] Donnelly N.J.; Bowman R.M.; Gregg J.M., Changes in functional behavior of 93% Pb (Mg1⁄3Nb2⁄3) O3− 7% PbTiO3 thin films induced by ac electric fields, *Phy. Rev. B*, **2006**;73:064110.